Integrated Prediction Method of Porosity Closure in Casting and Rolling Process for 8% Cr Die Steel

Junichi Nakagawa[1], Katsumasa Chiba[1], Yoshinori Sumi[1]

[1]Daido steel Co., Ltd.
30,2-Chome Daido-Cho Minami-Ku, Nagoya, Japan, 457-8545
Phone: +81-52-611-3894
Email: j-nakagawa@ac.daido.co.jp

ABSTRACT

In the production of special steel types, internal porosities caused by solidification shrinkage during casting can degrade the mechanical properties of the final product considerably. Therefore, ensuring complete closure of these porosities during forming processes is critical. While previous studies have examined porosity closure by using forging tests using artificial or process-derived defects, porosity formation behavior is highly dependent on the thermal and physical properties of each steel grade. To enable efficient laboratory-scale evaluation, our laboratory previously utilized the "Sato mold" to introduce controlled porosity defects into small ingots, facilitating the study of porosity closure by using unidirectional forging. This approach demonstrates effectiveness by using the Niyama parameter (an index of porosity formation) and the Q-value (an index of porosity closure) to assess residual porosity risk. In this study, we applied this methodology to 8% Cr die steel using bar-rolling tests, and conducted integrated casting and forming simulations to trace porosity evolution. The results confirm that the combined use of the Niyama parameter and Q-value can also be applied to evaluate residual porosity risks in rolling processes.

Keywords: Hot rolling, Sato mold, Die steel, Cast defect

INTRODUCTION

Internal porosities commonly arise during the production of specialty steel types owing to solidification shrinkage in the casting process. Comprehending the conditions that facilitate the closure of these porosities during plastic forming is crucial, as residual pores can undermine the mechanical properties of the final product. Previously published studies have predominantly examined the closure behavior of artificially introduced defects in laboratory-scale samples. Studies have been conducted in which pores of varying sizes were introduced into simple-shaped specimens, and the closure behavior under compression was compared between experiments and finite element analysis [1]–[5]. In addition, numerous investigations have examined closure behavior in various manufacturing processes that simulate actual components, such as hot extrusion [6], forging [7]–[11], and rolling [12]–[14]. Nevertheless, the intricate and diverse geometries of porosities in actual ingots, shaped by the specific attributes of various steel grades, may not align with the closure dynamics of these artificial defects. This discrepancy underscores the necessity for a more versatile and practical approach to investigate porosity closure across different steel types.

Addressing this need, the current study presents a systematic testing methodology that integrates both casting and plastic forming processes to assess porosity formation and closure behavior [15]–[17]. This approach utilizes small-scale ingots fabricated with a custom-designed mold that meticulously controls the shape and distribution of porosities [18]. The closure behavior of these porosities is examined based on bar-rolling tests coupled with comprehensive microstructural analyses of the ingots. Furthermore, casting simulations and finite element analyses of bar-rolling were employed to replicate the experimental conditions and provide in-depth insights into the factors influencing the porosity closure during casting and bar-rolling processes.

EXPERIMENTAL

2.1 Preparation of Ingot Samples

In this study, 8% Cr die steel was selected for casting experiments, with its specific chemical composition described in Table 1. The experimental setup is illustrated in Figure 1. In this system, molten steel is first transferred into a tundish and subsequently poured into a modified Sato mold via a sprue. This mold design adapts the original Sato mold [18] by incorporating three insulating porous refractory rings (A) and one mullite refractory chill ring (B). The modified split mold structure is based on the experimental framework developed by Sumi et al. [19]. The porous refractory and mullite chill ring exhibit thermal conductivities of 0.09 W/(m·K) and 4.2 W/(m·K), respectively. This mold design was engineered to promote porosity formation by inducing preferential solidification in the mullite refractory section (B), thereby interrupting the liquid phase supply.

The liquidus and solidus temperatures of the steel were calculated using Thermocalc™—a commercial phase diagram calculation software—and the target casting temperature was set at 220 K above the liquidus temperature. Figure 2 illustrates the resulting ingot shape postcasting, comprising a main ingot body (58 mm × 58 mm × 200 mm) and a hot-top section. In total, five ingots were cast for experimentation. One ingot was employed to examine the longitudinal distribution of porosities, while the remaining four underwent bar-rolling tests with varying reductions in area. These experiments provided critical insights into the formation and closure behavior of porosities during the casting and bar-rolling processes.

Table 1. Target composition of 8% Cr-die steel (mass%)

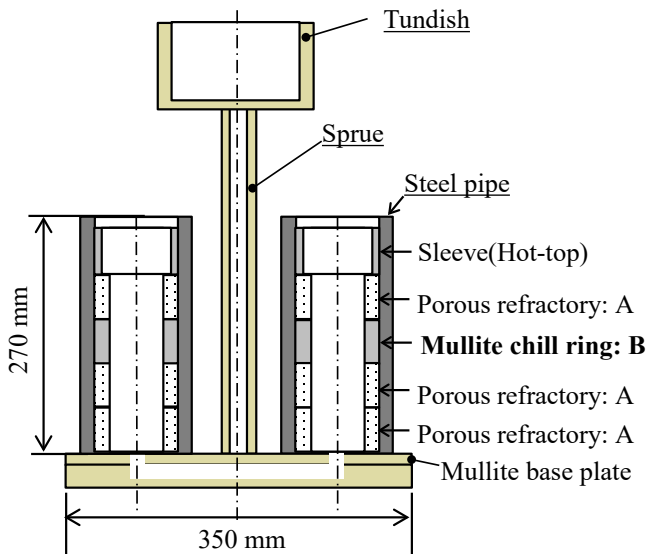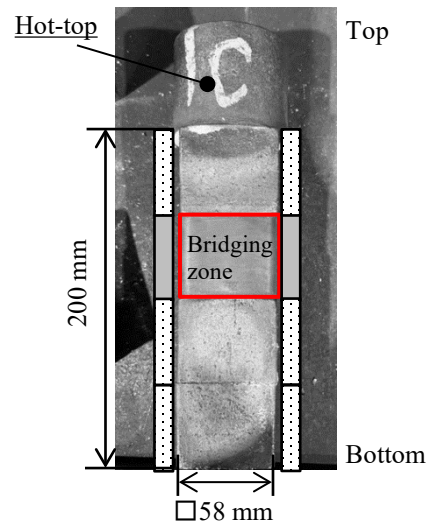| Element	C	Si	Mn	Cr	Mo	V	Fe
Target value	1.0	0.9	0.4	8.0	1.8	0.2	Bal.

Figure 1. Schematic of modified-Sato mold

Figure 2. Exterior photo of ingot

2.2 Methodology for Investigating Porosity Shape and Rolling Sample Preparation

To assess porosity morphology, a single sample was sectioned perpendicularly along its central axis. This section was subjected to macroscopic examination followed by penetrant testing to evaluate accurately porosity characteristics. In contrast, the other ingots were prepared using a different methodology in bar-rolling experiments. Each ingot was uniformly milled to remove 9 mm of material from all external surfaces and then cut to a length of 100 mm from the base.

Before initiating the rolling process, a nondestructive examination of the internal porosity shapes in each ingot was conducted using immersion ultrasonic testing. This technique provided valuable insights into the internal structure without compromising the integrity of the ingot. Figure 3 displays cross-sectional photographs of the as-cast and rolled samples, illustrating the preparation steps and setup for subsequent bar-rolling tests.
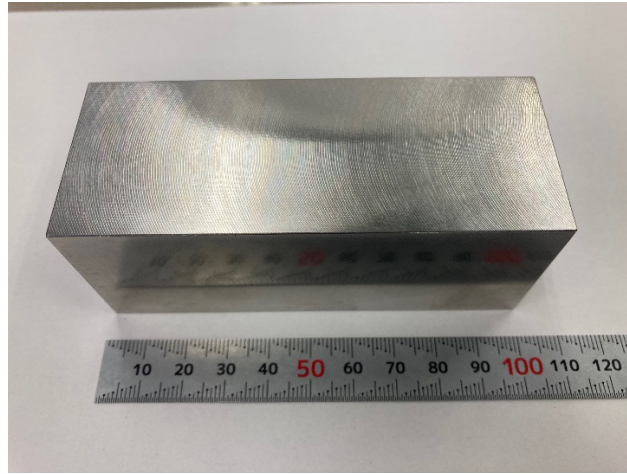
Figure 3. (a) Cross-sectional photograph of as cast, and (b) exterior photograph of rolling sample.

2.3 Hot-Rolling Test

Table 2 outlines the hot-rolling conditions applied to each ingot in this study, with detailed illustrations provided in Figure 4. The hot-rolling experiments were conducted at 1150 °C using a bar-rolling mill. The roll design included multiple grooves, allowing the material to be progressively reduced in size as it passed through each stage. Additionally, the material was rotated 90° after each pass.

During the preliminary phase of the experiment, all ingots were heated to 1150 °C in an electric furnace. Immediately after heating, each ingot was transferred to the rolling mill. To minimize temperature loss during rolling, the material was reheated in the electric furnace after every two passes, maintaining a 10-min heating cycle before returning to the rolling mill. When the rolling passes were completed, the material was allowed to air-cool. The rolling was performed unidirectionally, systematically progressing from the bottom (Bot) to the top (Top) of each ingot.

To evaluate porosity closure behavior, the reduction of area was varied systematically between 53.2% and 82.3%, defined as follows:

$$Reduction\ of\ area = \frac{A_0 - A_d}{A_0} \times 100 \tag{1}$$

where A_o and A_d represent the original and deformed cross-sectional areas, respectively. This experimental configuration provided precise control over rolling conditions, offering valuable insights into the relationship between reduction of area and porosity closure.

Table 2. Hot-rolling conditions

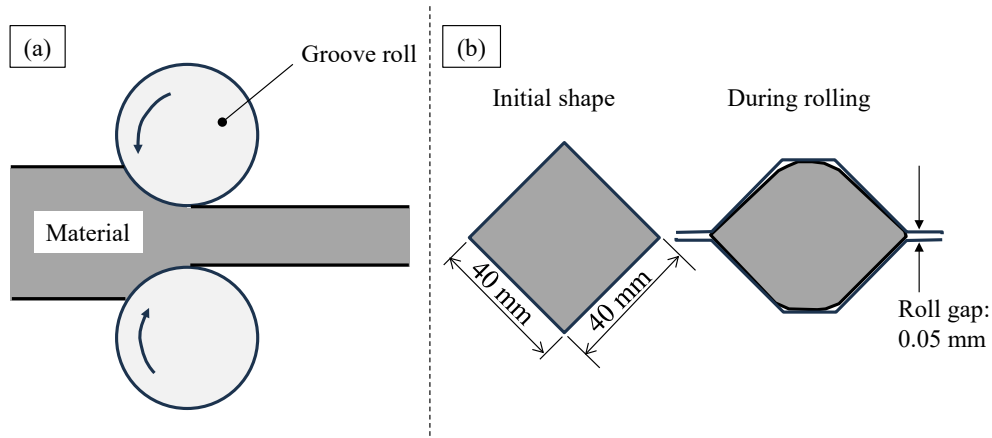| Sample number	Number of rotations [revolutions per minute]	Rotation speed [m/min]	Reduction of area [%]	Number of passes	Width after rolling [mm]
A	23.9	30	53.2	5	28.7
B			61.9	6	25.9
C			68.8	7	23.5
D			82.3	10	17.5

Figure 4. (a) Schematic of hot rolling at side view, and (b) front view of material.

2.4 Investigation of Porosity Closure Behavior After Rolling

Each rolled sample was longitudinally sectioned along its central axis for detailed examination. The investigation of porosity closure involved macroscopic observation and penetrant testing of these cross-sections. In areas where unclosed porosities were identified, microscopic analysis was conducted to characterize their features. Additionally, the area ratio of unclosed porosities was calculated to assess quantitatively their extent within the samples. This comprehensive methodology enabled a thorough evaluation of the effectiveness of the rolling process in achieving porosity closure.

2.5 Evaluation of Porosity Closure Behavior by Cooperation of Casting and Bar-Rolling Simulation

The porosity closure behavior was assessed using an integrated simulation approach that merges casting and plastic forming analyses. Porosity formation was evaluated by computing the Niyama criterion [20] with the casting simulation software THERCAST®, which is a 3D finite-element software for foundry processes such as ingot casting processes. The Niyama criterion is defined as follows,

$$N_y = \frac{G}{\sqrt{R}} \tag{2}$$

where G represents the temperature gradient during solidification, and R denotes the cooling rate in the same phase.

To evaluate porosity closure during forging, the ingot model, including its Niyama criterion distribution, was imported into the rolling simulation software TRANSVALOR MATERIAL FORMING, which is a 3D finite-element software for plastic forming, such as forging, rolling, etc. This integration enables the visualization of the Niyama criterion distribution based on metal flow during forging. Simultaneously, the porosity closure parameter, known as the Q-value [21], was also calculated as follows,

$$Q = \int_0^{\varepsilon_f} \left(-\frac{\sigma_m}{\sigma_{eq}}\right) d\varepsilon_{eq} \tag{3}$$

where σ_m and σ_{eq} denote the hydrostatic and equivalent stress, respectively, and ε_{eq} and ε_f represent the equivalent strain pre- and post-rolling. This integrated simulation approach enabled a thorough understanding of porosity formation and closure mechanisms, highlighting the key factors that affect the effectiveness of casting and rolling processes.

EXPERIMENTAL RESULTS

3.1 Porosity Distribution Before Bar-Rolling

Figures 5(a) and 5(b) display macroscopic photographs and penetrant test results of the longitudinal section, respectively. These images demonstrate the development of fine porosities just below the preferential cooling zone formed by the mullite chill ring. The results of immersion ultrasonic tests on various samples are illustrated in Figure 5(c), where the white regions indicate reflective sources. The similarity in the morphology of these reflective sources across multiple samples confirms the consistent porosity distribution before rolling in each specimen.
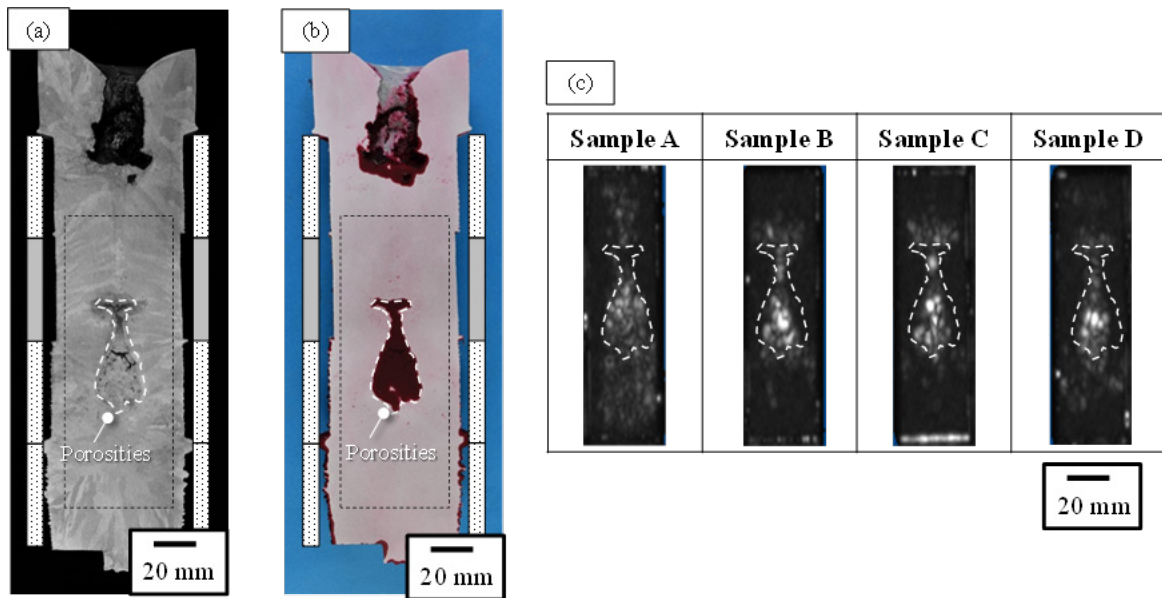
Figure 5. Photographs showing the (a) macrostructure and (b) penetrant test results. (c) Immersion ultrasonic test outcomes.

3.2 Porosity Closure Evaluation Results

Figure 6 displays macrostructural photographs of cross-sections at various area reductions. At the area reductions of 53.2%, 61.9%, and 68.8%, the elongation of porosity clusters in the longitudinal central region was observed. However, at an area reduction of 82.3%, no porosity clusters were detected in the longitudinal central region. Figure 7 shows cross-sectional photographs from penetrant tests at each area reduction level. Porosity was present in the central region (at an area reduction of 53.2%, subsequently diminished at 61.9%), but was not detected at area reductions of ≥68.8%. This analysis demonstrates a decrease in the extent of porosity at increasing area reductions, culminating in the absence of porosities at an area reduction of 82.3%. Figure 8 presents a micrograph highlighting the porosity area in more detail. The observations of the longitudinal central region revealed large porosities at area reductions of 53.2% and 61.9%. Their area ratios of porosity were 22.6% and 19.1%, respectively. As the reduction of area increased to 68.8%, porosity sizes decreased, and at 82.3%, porosities completely disappeared. Subsequently, at a position at one quarter of the length along the longitudinal direction, multiple porosities smaller than 100 μm were observed within the field of view at area reductions of 53.2% and 61.9%. At area reductions of 68.8% or higher, porosities were absent, confirming their compression. Moreover, the photograph of the microstructure supports this trend; as the reduction rate increases, porosity size decreases.
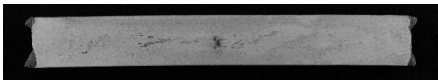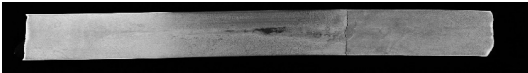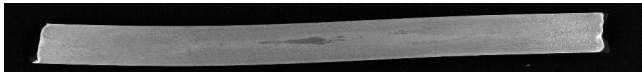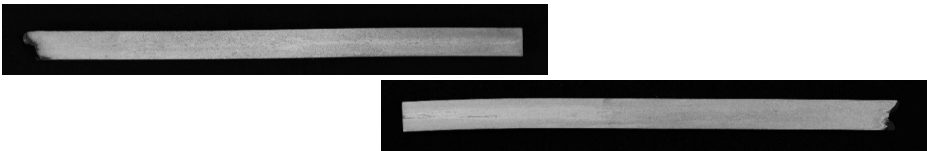
	Reduction of area	Cross-sectional photograph		
Sample A	**53.2%**	Top		Bottom
Sample B	**61.9%**			
Sample C	**68.8%**			
Sample D	**82.3%**			

Figure 6. Macrostructural photographs of cross-sections at all studied area reductions.
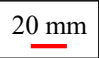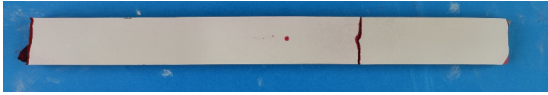
	Reduction of area	Cross-sectional photograph		
Sample A	**53.2%**	Top	20 mm	Bottom
Sample B	**61.9%**			
Sample C	**68.8%**			
Sample D	**82.3%**			

Figure 7. Penetrant test photographs of cross-sections at all studied area reductions.
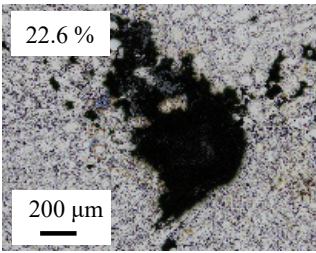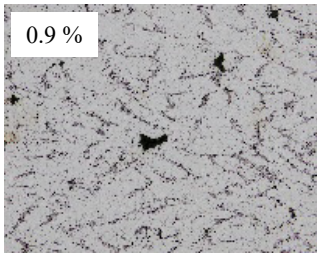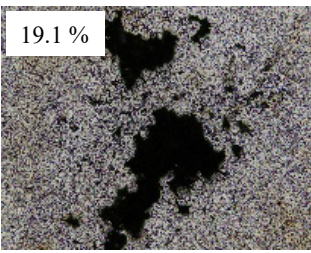
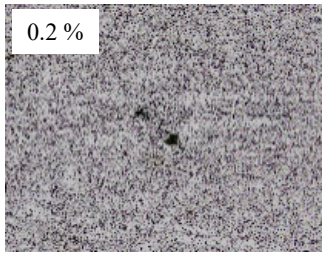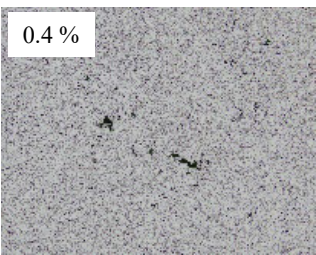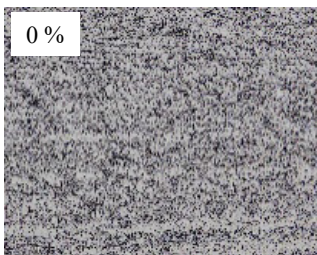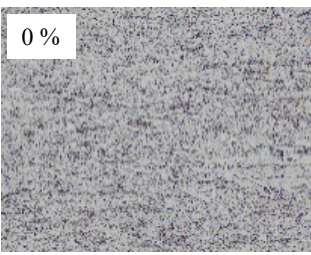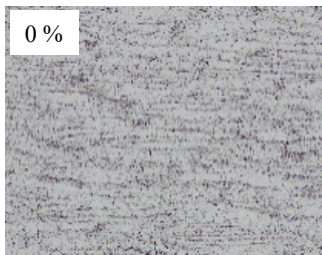| (1) Sample A : Reduction=53.2%		(2) Sample B : Reduction=61.9%	
Longitudinal center	one-quarter of the length	Longitudinal center	one-quarter of the length
22.6 % 200 µm	0.9 %	19.1 %	0.2 %
(3) Sample C : Reduction=68.8%		(4) Sample D : Reduction=82.3%	
Longitudinal center	one-quarter of the length	Longitudinal center	one-quarter of the length
0.4 %	0 %	0 %	0 %

Figure 8: Microscopic observations of the longitudinal quarter positions.

3.3 Prediction of Porosity Generation Using Casting Simulations

Figure 9 compares the Niyama criterion contour in a casting simulation with the observed porosity distribution in the samples. The analysis reveals that porosities primarily form in regions where the Niyama criterion is approximately equal to 1.67 or lower. This porosity formation threshold aligns with previously reported values for 8% Cr die steel, which range from 1.6 to 2.9 [22]. These results further validate the Niyama criterion's effectiveness as a predictive index for porosity formation during solidification.
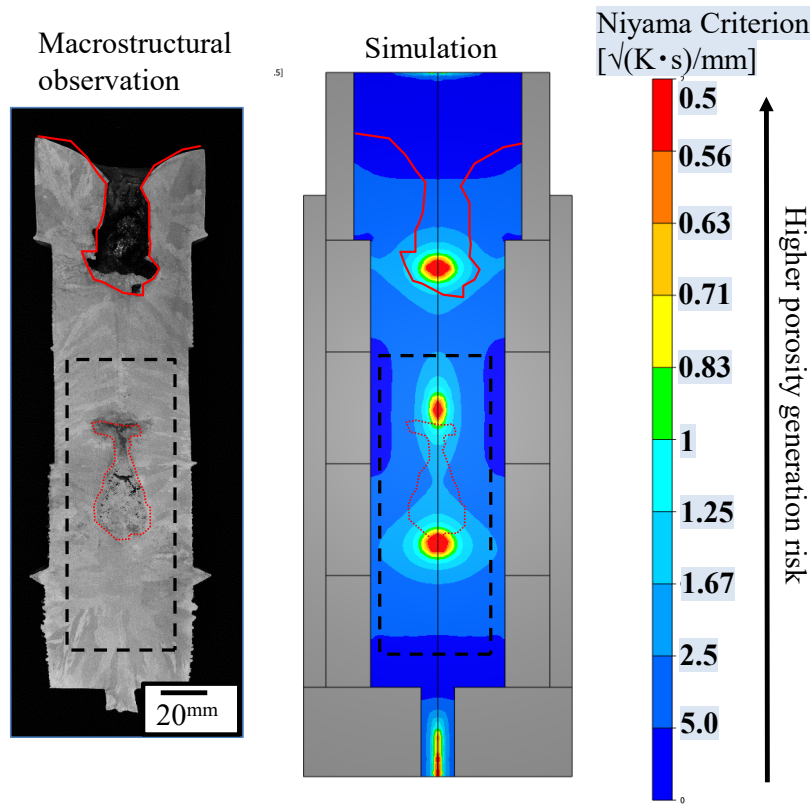
Figure 9. Macrostructural image and simulation contour plot of the Niyama criterion.

3.4 Rolling Simulation Results

Figure 10 displays the simulation's contour plot after five passes. The analysis conditions were as follows: ambient temperature at 25 °C, roll temperature at 50 °C, Coulomb friction coefficient of 0.3, heat transfer coefficients of 2.0 kW/m²K (between the roll and material) and 0.15 kW/m²K (between the atmosphere and material). Figure 11 presents the Q-value for each area reduction in the longitudinal cross-section. As the reduction rate increased, both strain and stress intensified, leading to a higher Q-value. Additionally, the Q-value tended to be higher in areas closer to the surface compared with the central region.

Figure 10. Appearance of rolling simulation.

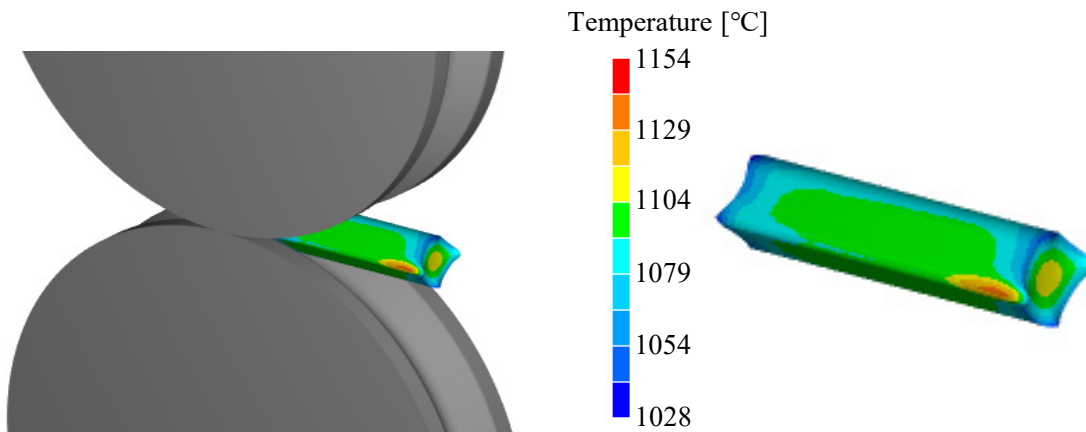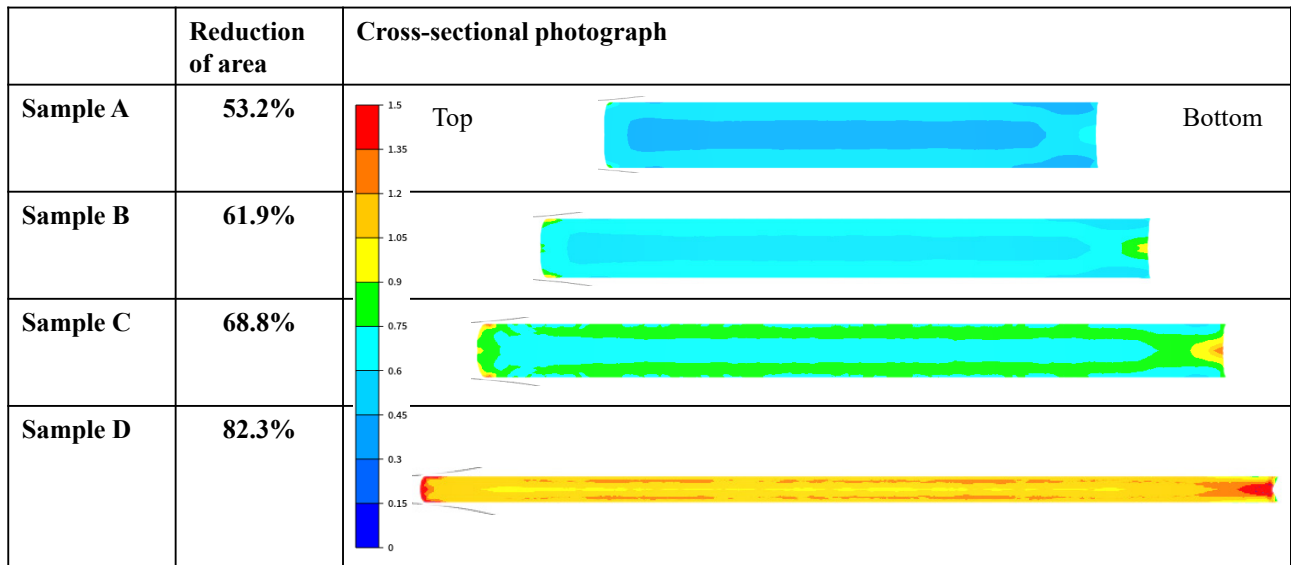|	Reduction of area	Cross-sectional photograph
Sample A	53.2%	Top ... Bottom
Sample B	61.9%	
Sample C	68.8%	
Sample D	82.3%	

Figure 11. Q-values at all tested area reductions in the longitudinal cross-section.

3.5 Comparison of Niyama Criterion and Q-Values

Figure 12 illustrates the Niyama index and Q-values at the reduction rates of 53.2% and 82.3%, emphasizing the microporosity on the bottom side. In Figure 12(a), at a reduction rate of 53.2%, the Niyama criterion decreases between 150 and 170 mm from the top edge, indicating a major porosity formation risk. The Q-value remains at ~0.4 and gradually increases from ~190 mm toward the bottom side. Conversely, Figure 12(b) displays that at an 82.3% reduction rate, the Niyama criterion decreases by 410–460 mm from the top edge. In this case, the Q-value is ~1.0 and increases at distances located at ~550 mm from the top edge.
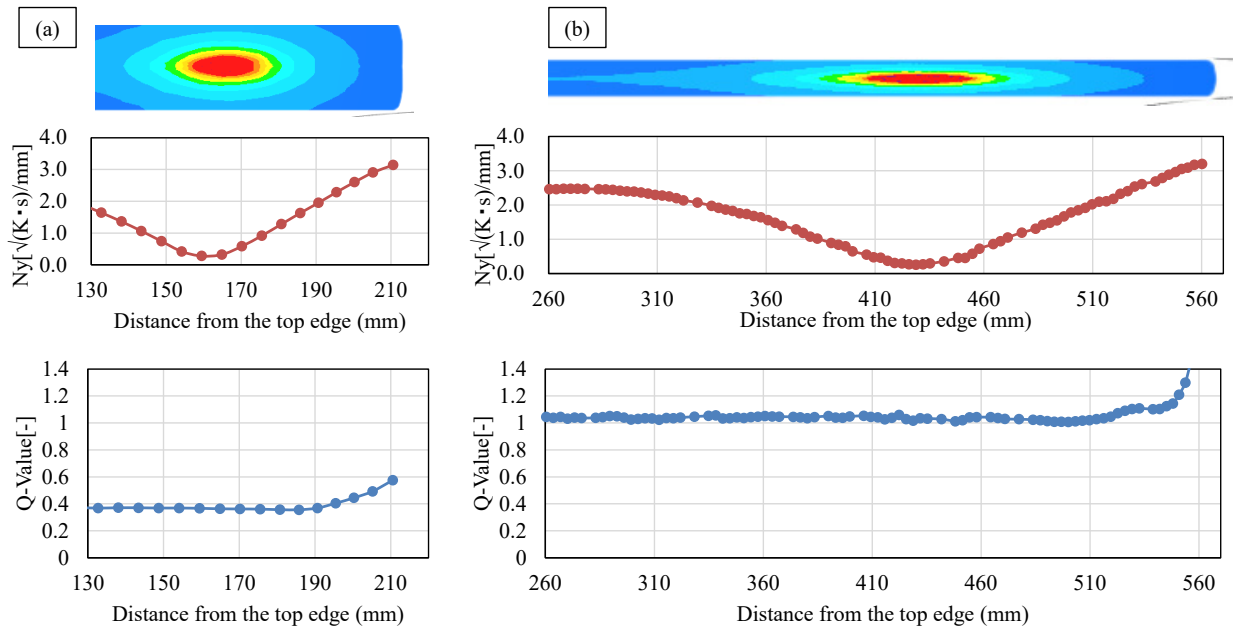
Figure 12. Comparisons of Niyama criterion index and Q-value.

DISCUSSION

4.1 Evaluation of Porosity Closure Conditions Based on the Niyama Criterion and Q-Value

Figure 13 consolidates the conditions for porosity closure by considering both the Niyama criterion and Q-value. The correlation between the Niyama criterion and Q-value at various points along the sample's central axis is plotted at all reduction areas. Regions where porosity persists are marked with the symbol "×," and those without pores are marked with the symbol

"○" based on microscopic observations. The findings indicate that in regions with a high propensity for porosity formation in the as-cast state—namely, areas with low Niyama criterion index values—a higher Q-value is required to achieve porosity closure. Conversely, in regions with high Niyama criterion index values, porosity closure is possible at lower Q-values. We quantified the porosity closure threshold using the obtained plots, and confirmed that it can be approximately described by the following equation:

$$\frac{N_y}{Q^{-2.0}} \geq 0.25 \tag{4}$$

We present the porosity crimping prediction formula for forging tests conducted with the same specimens used in this study [4].

$$\frac{N_y}{Q^{-1.0}} \geq 0.25 \tag{5}$$

Additionally, previous research investigating porosity crimping behavior with Sato molds in forging found that voids were almost fully crimped at a Q-value of approximately 0.6. In contrast, during rolling, voids did not completely close at the same Q-value. Furthermore, the following equation [based on Equations (4) and (5)] holds.

$$\frac{N_y}{Q^{-m}} \geq 0.25 \tag{6}$$

Herein, m denotes a coefficient accounting for various factors, including porosity shape, quantity, and compression direction. The porosity closure threshold varies depending on the shape of porosity. Accurate prediction of porosity size enables a more precise determination of the closure threshold. Therefore, we derived the porosity size using the Niyama criterion, which indicates the risk of porosity formation. Initially, the pressures from the liquid phase $P = (P_o - \Delta P)$, surface tension $\frac{2\sigma_{LG}}{r}$, and the gas bubble pressure P_{gas} are balanced; accordingly, the following equation holds true [23],

$$P_0 - \Delta P = P_{gas} - \frac{2\sigma_{LG}}{r} n \tag{7}$$

where P_o represents the pressure liquid at the liquidus temperature, ΔP denotes the pressure gradient, σ indicates the surface stress of the porosity, and r indicates the pore radius. The pressure gradient can be expressed by Equation (8),

$$\Delta P = \frac{\mu f_l \beta'(T_c - T_s)}{K} \cdot \left(\frac{G}{\sqrt{R}}\right)^{-2} = \frac{\mu f_l \beta'(T_c - T_s)}{K} \cdot \left(N_y\right)^{-2} \tag{8}$$

where T_s refers to the solidus temperature, T_c represents the temperature at the typical point in the position between the root and the tip of the dendrite, μ denotes the viscosity of the liquid phase, f_L indicates the liquid fraction, and $\beta' = \frac{\beta}{(1-\beta)}$ corresponds to the solidification shrinkage ratio. Subsequently, Equation (8) was integrated into Equation (7) to determine the pore radius r.

$$r = -\frac{2\sigma_{LG}}{\left(P_0 - \frac{\mu f_l \beta'(T_c - T_s)}{K} \cdot \left(N_y\right)^{-2} - P_{gas}\right)} = -\left(C_1 - C_2 N_y^{-2}\right) \tag{9}$$

For the purposes of this derivation, C_1 and C_2 were assumed to be constant. Rearranging Equation (9) to express N_y, the following expression is derived,

$$N_y = \frac{C_1}{r + C_2} \tag{10}$$

Finally, the expression of parameter N_y [see Equation (6)] was substituted into Equation (10), leading to the derivation of the subsequent equation,

$$\frac{C_1/(r + C_2)}{Q^{-m}} \geq 0.25 \tag{11}$$

Equation (11) establishes a new threshold to assess whether porosity closure occurs, based on porosity geometry and its propensity to close. By predicting the porosity size using the Niyama criterion, it is possible to derive a Q-value that accounts for porosity dimensions. Additionally, future research will examine the porosity aspect ratio, determine the m-value based on simulations, and develop a more comprehensive and practical predictive equation.
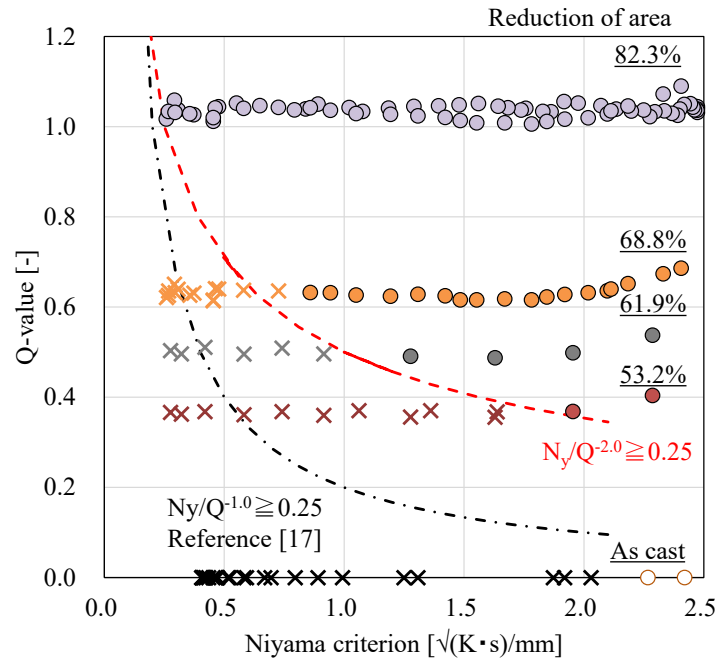

Figure 13. Evaluation of porosity closure conditions using the Niyama criterion index and Q-value.

4.2 Mechanism of Porosity Closure for Plastic Forming

Figure 14 illustrates the mechanism of porosity crimping during rolling with and without rotation. In the absence of rotation, compression was applied from a single direction, causing the porosity to crimp once a specific compression threshold was reached. In contrast, with rotation, after being compressed from one direction, additional compression was applied from the opposite direction at 90°, causing the partially closed pores to open. Repeated processing complicates porosity closure compared with forging or rolling in conjunction with unidirectional compression [24]. Zhang et al. investigated the relationship between porosity size and the degree of compression [25]. In addition, Peng et al. conducted experiments using specimens subjected to different heat treatment temperatures to examine the effects of temperature [26]. To improve further the accuracy of porosity closure predictions, it will be necessary to formulate a model that considers multiple parameters, such as porosity size, shape, and diffusion phenomena influenced by temperature.
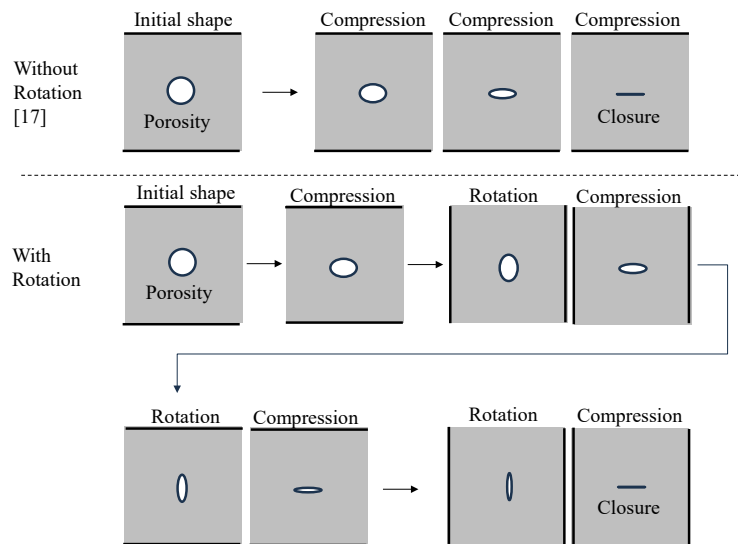

Figure 14. Schematics showing the mechanism of porosity closure with and without rotation.

CONCLUSIONS

Die steel ingots (8%-Cr) containing fine porosities, fabricated using a modified Sato mold, were subjected to hot-rolling tests to examine the porosity-closure behavior at varying pressure drop rates. Simultaneously, casting and rolling simulations were performed to replicate these experiments. The effectiveness of porosity closure was evaluated using the Niyama criterion and Q-values. The major conclusions of this study are listed below:

- Fine porosity sizes diminished as the reduction rate increased; notably, at an area reduction of 82.3%, all porosities were entirely closed.
- In forging experiments, porosity closure was achieved when the Q-value was approximately 0.6 or higher, whereas in the present rolling experiments, porosity closure required a Q-value of approximately 1.0 or higher. Repeated processing complicates porosity closure compared with forging or rolling in conjunction with unidirectional compression.
- The porosity size was defined using the Niyama criterion, and its relationship with the Q-value was formulated from the experimental results, the threshold value was determined to be at least 0.25.
- Future research aims to incorporate factors such as the porosity aspect ratio and temperature into predictive equations to establish a comprehensive and practically applicable predictive model.

REFERENCES

1. Kakimoto et al., Journal of Materials Processing Technology, 2010, Vol. 210, pp 415–422.

2. Kishimoto et al., Sosei to kakou, Japan, 2019, Vol. 60, pp 167.

3. Chen et al., Computational Materials Science, 2014, Vol. 91, pp 303–309.

4. Kim et al., Journal of Materials Research and Technology, 2025, Vol. 36, pp 6802–6820.

5. Saby et al., Finite Elements in Analysis and Design, 2015, Vol 105, pp 63–78.

6. Afrasiab et al., Mechanics Research Communications, 2022, Vol. 124, p 103971.

7. Harris et al., Journal of Manufacturing Process, 2017, Vol. 26, pp 131–141.

8. Kim et al., Journal of Materials Processing Technology, 2011, Vol. 211, pp 1005–1013.

9. Lee et al., Journal of Materials Processing Technology, 2011, Vol. 211, pp 1136–1145.

10. Feng et al., Journal of Materials Processing Technology, 2016, Vol. 237, pp 371–385.

11. Chen et al., International Journal of Plasticity, 2013, Vol. 49, pp 53–70.

12. Huang et al., Journal of Iron and Steel Research, 2014, Vol. 21(3), pp 287–294.

13. Faini F et al., Journal of Materials Processing Technology, 2018, Vol. 259, pp 235–242.

14. Czempas et al., Advances in Industrial and Manufacturing Engineering, 2024, Vol. 8, p 100134.

15. Tsuji et al., Denkiseiko, Japan, 2021, Vol. 92, p 45.

16. Chiba et al., IFM-120, Italy, 2024.

17. Chiba et al., Denkiseiko, Japan, 2024, Vol. 95, p 39.

18. Sato et al., Tetsu to Hagane, Japan, 2013, Vol. 99, p 108.

19. Sumi et al., ISIJ International, Japan, 2023, p 1131.

20. Niyama et al., 49th World Foundry Congress, 1982, p 10.

21. Araki et al., Japanese Spring Conference for the Technology of Plasticity, Japan, 1986, p 383.

22. Sumi et al., CAMP-ISIJ, Vol. 36, Japan, 2023, p 429.

23. Yasuda, Gyoko kogaku no kiso, UCHIDA ROKAKUHO PUBRISHING CO., LTD., Japan, 2022, p 208.

24. Zhang et al., Procedia Engineering, 2017, Vol. 207, pp532–537.

25. Zhang et al., Journal of Material Processing Technology, 2009, Vol. 209, pp 1950–1959

26. Y. Peng et al., Journal of Material Processing Technology, 2024, Vol. 324, p 118267.